Tobias Laux , Khong Wui Gan , Janice M. Dulieu-Barton , Ole T. Thomsen , A simple nonlinear constitutive model based on non-associative plasticity for UD composites: development and calibration using a Modified Arcan Fixture, *International Journal of Solids and Structures* (2018), doi: https://doi.org/10.1016/j.ijsolstr.2018.12.004

A simple nonlinear constitutive model based on non-associative plasticity for UD composites: development and calibration using a Modified Arcan Fixture

Tobias Laux [a], Khong Wui Gan [a,b], Janice M. Dulieu-Barton [a], Ole T. Thomsen [a]

[a] Faculty of Engineering and the Environment, University of Southampton, Highfield, SO17 1BJ, Southampton, UK

[b] Faculty of Engineering and the Environment, University of Southampton Malaysia, Kota Ilmu Educity @ Iskandar, 79200 Iskandar Puteri, Johor, Malaysia

Keywords: Composites, Multiaxial loading, Nonlinear constitutive model, Non-associative plasticity, Modified Arcan Fixture (MAF)

Abstract

A simple nonlinear constitutive model based on non-associative plasticity for unidirectional (UD) composites is developed and calibrated using a Modified Arcan Fixture (MAF) and Digital Image Correlation (DIC). The plasticity model accounts for the nonlinear response of unidirectional composites subjected to multiaxial loading, assuming transverse isotropy and negligible plasticity in the fibre direction. The different responses in transverse tension and compression are accounted for by a Drucker-Prager type yield function to include transverse pressure sensitivity. It is shown that using an associative flow rule leads to the prediction of non-physical plastic strain components, whilst the use of a non-associative flow rule resolves the deficiency of the associative model. The non-associative model is calibrated and verified against biaxial test data obtained from glass/epoxy specimens using the MAF, as well as against off-axis test data available in the literature for two additional composite material systems. The nonlinear stress-strain curves for unidirectional composites subjected to multiaxial stress states predicted by the model are in good agreement with all three sets of experimental data, thus demonstrating the predictive capabilities of the proposed model.

1 Introduction

Unidirectional (UD) fibre reinforced polymers (*e.g.* glass/epoxy and carbon/epoxy) are widely used in primary structures across many industrial sectors due to their high specific stiffness and strength [1]. UD composites are strongly anisotropic and often exhibit nonlinear and pressure sensitive behaviour when subjected to multiaxial stress states, especially in shear and transverse compression.

The nonlinear behaviour is due to different physical effects that include plasticity (in polymer resin), micro-crack formation and geometric nonlinearity (*e.g.* fibre rotation) [2].

The modelling framework of plasticity was used by several researchers to cumulatively account for these nonlinear effects. Following on from this, the terminology 'plastic' and 'plasticity' is used in this paper to conveniently represent the cumulative nonlinear material response due to plasticity, micro-cracking and geometric nonlinearity, and not only strictly physically plastic behaviour. Sun and Chen [3], for example, developed a one-parameter associative plasticity model to simulate the response of UD composites subjected to multiaxial loading where the material behaviour is plastic in transverse and shear loading and linear elastic in the fibre direction. In an associative model, the plastic strain tensor is assumed to be normal to the yield surface, whereas in a non-associative model the plastic strain tensor is assumed to be normal to a potential function, which is different from the yield function. The associative model predictions in [3] agreed well with the measured nonlinear response of boron/epoxy and carbon/epoxy specimens in off-axis tensile tests. Noting that the transverse stress-strain behaviour in tension and compression is distinctly different, and that the one-parameter quadratic yield function used in [3] could not account for the different stress-strain behaviour in tension and compression, Yokozeki *et al.* [2] extended the model by including a Drucker-Prager type [4] linear dependency of the hydrostatic pressure in the yield function. Despite the use of an associative flow rule, good agreement between model predictions and off-axis tensile and compressive test results were reported. Gan *et al*. [5] adopted a similar plasticity framework to predict the nonlinear biaxial response of carbon/epoxy subjected to combined through-thickness compression and interlaminar shear or longitudinal tension. The yield function in [5] was constructed based on the stress invariants for transversely isotropic material [6], [7], and assuming negligible plasticity in the fibre direction. In a UD composite (see Fig. 1), the transversely isotropic plane is perpendicular to the fibre direction (*1*- direction) and is spanned by the transverse (*2*- direction) and through-thickness (*3*- direction) material axes.

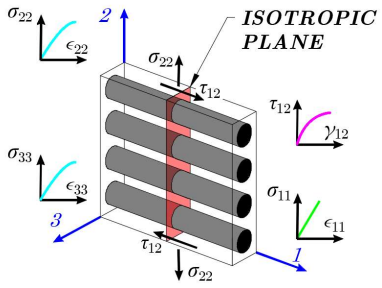

Fig. 1: Illustration of a UD composite element showing the isotropic plane [6], [7] *and the stress-strain behaviour parallel to the fibres, transverse to the fibres and in the through-thickness direction.*

All models discussed so far assume the existence of an intrinsic effective plastic stress-strain relationship (or hardening rule) independent of the stress state, which accounts for the cumulative nonlinearity in the transverse and shear stress-strain curves. In both [3] and [5] the shear stress-strain

curve was used to derive the effective plastic stress-strain relationship, whereas in [2] the effective plastic stress-strain relationship was obtained by collapsing all experimentally obtained effective plastic stress-strain curves at different off-axis angles into one 'master curve' using a least-squares optimisation procedure to determine the best fit yield and hardening parameters. These simple plasticity models discussed so far have adopted associative flow rules and isotropic hardening laws with a minimum number of plasticity parameters.

A more complex plasticity model, based on the stress invariants for a transversely isotropic material, was proposed by Vogler *et al*. [8], [9]. A non-associative flow rule was adopted, where the direction of the plastic flow was taken as the gradient of a plastic potential function that differs from the yield function as the pressure dependent yielding term is omitted. It was argued that the non-associative flow rule allows accurate prediction of the effective plastic Poisson's ratio and the volumetric plastic strains which is not possible with an associative model. The plasticity model was calibrated based on standard tests, hydrostatic pressure compression tests [10], and results from computational micromechanics due to the lack of appropriate experimental data. Often, the parameters were deduced by scaling from similar materials and the lack of multiaxial experimental data was emphasised as a major difficulty in calibrating the model. Vyas *et al.* [11] proposed a similar non-associative plasticity model to [8] which retained the linear hydrostatic pressure term in the plastic potential in a modified form to ensure an accurate representation of the effective plastic Poisson's ratio and volumetric strain. The model also accounted for stiffening of the elastic properties (transverse Young's modulus E_2 and shear modulus G_{12}) with applied hydrostatic pressure. The plasticity model was calibrated with biaxial experimental data obtained from filament wound tubular specimens subjected to shear and hydrostatic pressure [12] and off-axis tests under hydrostatic pressure [13]. Further, Hsu *et al*. [14] modelled the combined transverse compression and shear response of carbon/PEEK composites using a micromechanical finite element model where a non-associative Drucker-Prager type plasticity model was prescribed to the matrix. The PEEK matrix material model was calibrated by tests conducted on a custom designed biaxial testing facility using a standard test machine and an additional hydraulic actuator [15].

It can be concluded from the discussion above that multiaxial experimental data is needed to develop and calibrate nonlinear material models for UD composites. However, multiaxial data is rare due to the complexity involved in multiaxial testing and no consensus has been reached on a preferred experimental procedure to obtain such data.

The aim of the present paper is to develop a nonlinear, pressure sensitive constitutive model for UD composites under in-plane multiaxial loading that can be fully calibrated using a Modified Arcan Fixture (MAF) and Digital Image Correlation (DIC) [16]. The MAF [17] is a novel biaxial test rig which can be used in a standard test machine to characterise UD composites in the full combined

tension/shear (as is already possible with the original Arcan's rig [18]) and compression/shear stress domains using a single test fixture. Compression testing is enabled through the addition of anti-buckling rails which prevent out-of-plane displacements of the fixture. Compressive test data is crucial for this work because the most pronounced nonlinearities are observed in the transverse compression/shear stress domain. The relative simplicity of the MAF in comparison to alternatives such as using tubular specimens, conducting tests in a high-pressure apparatus, off-axis tests with a different specimen configuration for each biaxial stress state or the use of additional hydraulic actuators, makes it an ideal candidate for identification of biaxial material parameters and is thus addressing the lack of multiaxial experimental data in the literature. In addition, DIC allows acquisition of the complex full field strain maps of all in-plane strain components under multiaxial loading without the need for multiple strain gauges. The DIC strain measurements can conveniently be used in combination with the load output from the test machine to derive the stress-strain relationships.

The literature review has shown that current plasticity models, which assume transverse isotropy, neglect plasticity in the fibre direction and use a Drucker-Prager type yield function, generally are able to predict the nonlinear, pressure sensitive transverse and shear stress-strain curves in good agreement with experimental data. Most of the simple plasticity models (*e.g.* [2], [3] and [5]) have adopted associative flow rules, whilst others [8], [11], [14] adopted more complex non-associative flow rules. In the present paper it is demonstrated that the use of associative flow rules can lead to the predictions of non-physical inelastic transverse strains in UD composites subjected to shear-dominated combined transverse compression/shear stress states, and further that a Drucker-Prager type yield function is unsuitable for being used as a plastic (inelastic) potential function for UD composites. Here a simple nonlinear constitutive model similar to [2] and [5] is developed that is based on non-associative plasticity to account for the nonlinear transverse and shear stress-strain curves and pressure sensitive behaviours of UD composites. It is demonstrated how the MAF in combination with DIC is used to obtain the required biaxial experimental data to calibrate the nonlinear material model. The model is then applied to a RP-528 glass/epoxy prepreg system [19] characterised by the authors using the MAF [17] and also to off-axis test results available in the literature for two other material systems (T800/3633 carbon/epoxy [2] and infused glass/epoxy laminates [20]) to demonstrate its relevance. Further, the improved predictive capability of the proposed non-associative model is established by comparison with an associative plasticity model [2].

2 MAF/DIC biaxial experiment

2.1 Experimental set-up and procedures

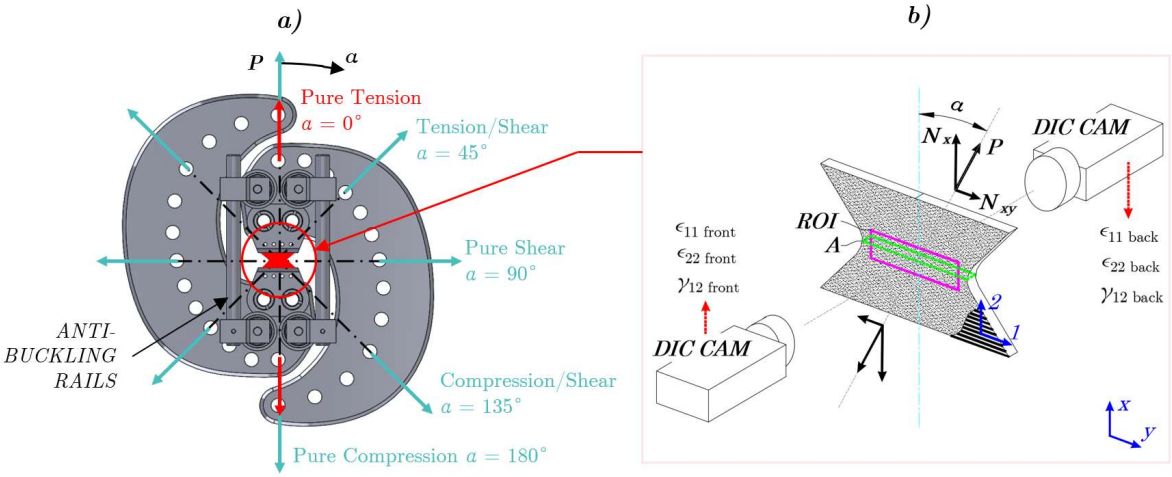

Fig. 2: Front view of the MAF (a) and the DIC set-up used to extract the average strains in the region of interest (ROI) in the gauge section of both sides of the specimen.

The front view of the MAF and the 'butterfly' specimen configuration used is shown in Fig. 2. Further details on the MAF and the experimental set-up can be found in [17]. The MAF can subject the specimens to different combined tension/shear and compression/shear stress states by varying the pairs of loading holes (designated by the angle α). The loading holes can be adjusted in increments of 15° from pure tension (α = 0°), over combined tension/shear (α = 15° to 75°), pure shear (α = 90°), combined compression/shear (α = 115° to 165°), to pure compression (α = 180°). The butterfly specimens were manufactured from 12 plies of E-glass/epoxy RP-528 UT300 E00 M32 prepreg supplied by PRF Composite Materials in UD stacks and were cured at 120° C and 6.2 bar according to the manufacturer's data sheet [19]. The butterfly specimen geometry with the fibre direction (*1*-axis in Fig. 2b) aligned parallel to the waistline was chosen to promote failure at the waisted gauge section. The gauge area, *A,* was on average 28.56 mm wide and 2.90 mm thick, the notch radius was 5 mm and the gauge length was 24 mm. The averaged biaxial stress state in the gauge section, comprising of transverse normal stress $\sigma_{22\,AVG}$ and shear stress $\tau_{12\,AVG}$, can be determined by the parameters shown in Fig. 2, *i.e.* the loading angle, α, the applied load, P, and the gauge area, A, as follows:

$$\sigma_{22AVG} = \frac{P}{A}\cos(\alpha) \tag{1}$$

$$\tau_{12AVG} = \frac{P}{A}\sin(\alpha) \tag{2}$$

To derive the stress-strain relationships under various biaxial stress states defined by α, the required stresses are calculated according to Equations (1) and (2), while the associated strains are obtained

using 2D DIC on both sides of the specimen (see Fig. 2b). The two-camera set-up allows convenient detection and correction of possible out-of-plane displacements of the rig and/or specimen, due to asymmetric loading or through-thickness material variations by averaging the strain values taken from the front and back faces of the specimens. It should be noted that there were little differences between the strain values obtained from the front and back faces. To perform the DIC the specimens were spray-painted with black speckles on a white background. Cameras were positioned approximately 750 mm away from the front and back sides of the specimen (see Fig. 2b); the DIC system specifications and parameters are summarised in Table 1.

Table 1: DIC system specifications and set-up.

Camera	5M Imager E-lite, La Vision
Sensor	12 bit, 2248 x 2050px
Lens	Sigma 105mm f2.8 EX DG Macro
Lightning	NILA ZAILA Led Lights
Imaging distance	~ 750 mm
Magnification	0.123
Pixel resolution	~ 1px = 22μm
DIC Software	La Vision DaVis 8.3.1
Subset Size	51 px
Step Size	25 px
Sub-pixel interpolation	6th order spline
Smoothing	None

An example of a DIC strain map obtained on a specimen loaded in pure shear is shown in Fig. 3. The strains used to derive the stress-strain relationship were averaged over a region in the waisted gauge area denoted as the ROI as shown in Fig. 2b and Fig. 3. The ROI spans the whole gauge width, only avoiding the measurement points closest to the edges of the specimens where the strain measurement is inaccurate due to the numerical treatment of the edges. The ROI spans the whole width of the gauge section to obtain the average gauge section strains, which are associated with the average gauge section stresses obtained by Equation (1) and (2). The ROI is approximately 50 pixels wide and 3 pixels high (slightly different from specimen to specimen due to variations in magnification). In DIC, the subset is defined as the region over which the displacement is evaluated by the correlation algorithm, while the step size defines the amount the subsets overlap [16].

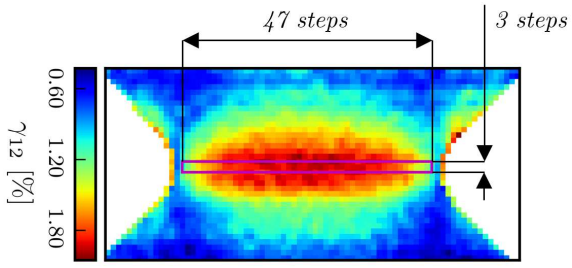

Fig.3: Example DIC strain map with the ROI (purple box) indicated for a specimen loaded in pure shear.

Having extracted the averaged strain in the ROI on both sides of the specimen, the strains used to construct the stress-strain curves are obtained as the average of the front and back strains, *i.e.* $\epsilon_{22\,front}$ and ϵ_{22back} .

$$\epsilon_{22AVG} = \frac{1}{2}(\epsilon_{22\,front} + \epsilon_{22back}) \tag{3}$$

$$\gamma_{12AVG} = \frac{1}{2}(\gamma_{12\,front} + \gamma_{12back}) \tag{4}$$

Three specimens per loading angle were tested for α = 0°, 30°, 45°, 90°, 120°, 150° and 180° and two for α = 135° and 165°. A single extracted representative stress-strain curve was then obtained by fitting a polynomial function through all the experimental stress-strain curves acquired for each loading angle α.

2.2 Experimental results and discussion

Fig. 4 shows the extracted representative stress-strain curves obtained using the MAF and DIC according to the experimental procedure outlined in Section 2.1 for all tested loading angles; Fig. 4 a and b show the transverse (σ_{22} versus ϵ_{22}) and shear (τ_{12} versus γ_{12}) stress-strain curves under tensile loading, while Fig. 4 c and d show the transverse and shear stress-strain curves under compressive loading.

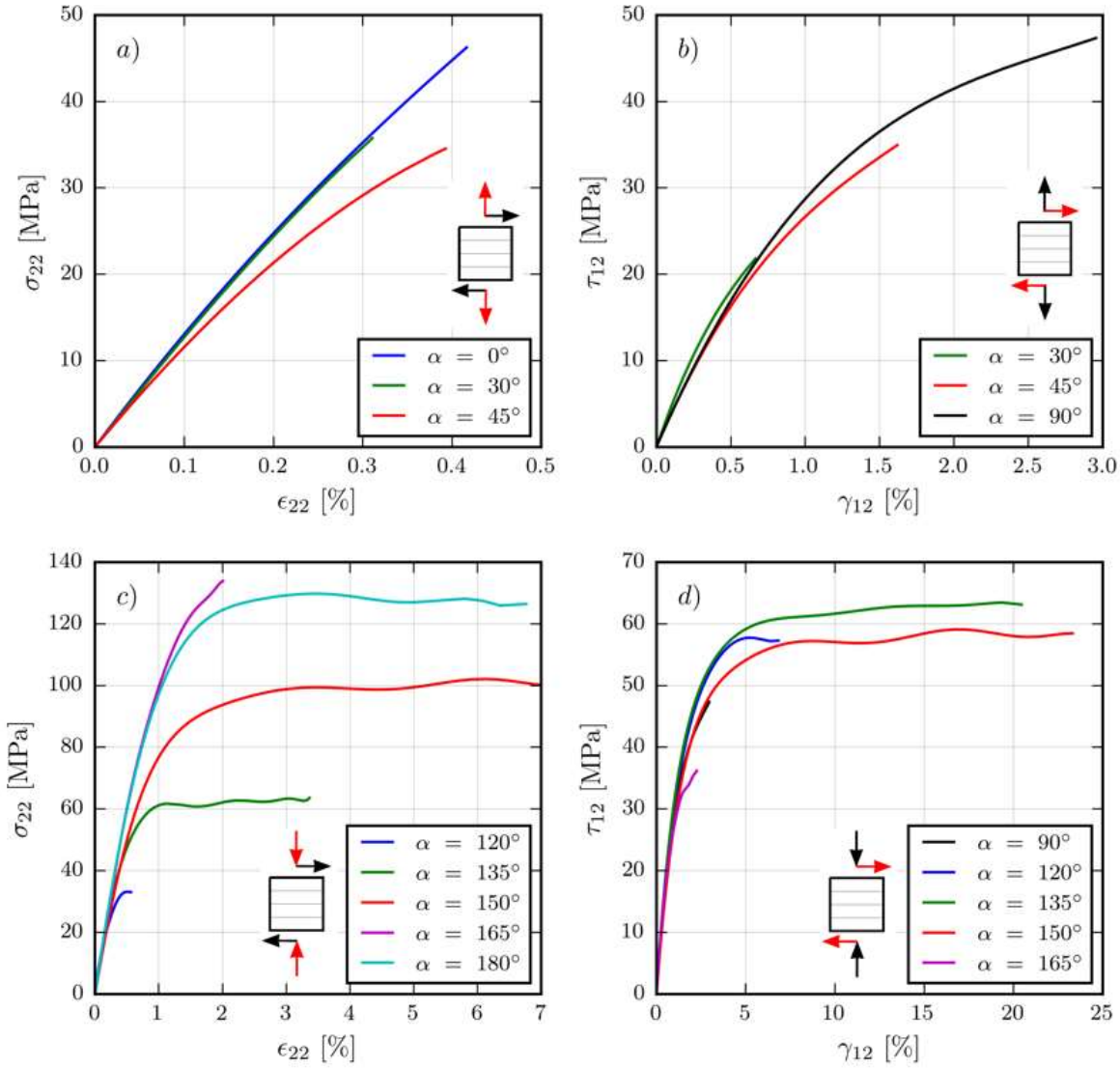

Fig. 4: Transverse (a and b) and shear (c and d) stress-strain curves obtained with the MAF for different stress states.

Fig. 4a shows that the transverse stress-strain responses to combined tension/shear stress states are almost linear, but become more nonlinear as the loading angle α increases. It is also noted that the transverse modulus is reduced with increasing *α*. Fig. 4b shows that the shear stress-strain curves obtained for combined tension/shear stress states are nonlinear from the moment shear stress is applied, *i.e.* a distinct yield point is not evident. On the other hand, the transverse compressive normal stress-strain curves are initially linear followed by a strongly nonlinear zone before a plateau stress is reached as shown in Fig. 4c. It is further observed that very large transverse compressive strains are developed before ultimate failure occurs for intermediate combined compression/shear stress states (α = 135°-165°). Fig. 4d shows that the shear failure stress initially increases with modest compressive transverse stress (α = 120°-135°) before it starts to drop for α = 150°-165°. This supports the predictions by inter-fibre failure theories such as Cuntze's [21], Puck's [22],[23] or LaRC [24], which account for this shear strength enhancement effect when moderate transverse

pressure (compression) is applied. The shear stress-strain curves for α = 120° to 150° feature a distinct plateau stress and have very large strains to final failure (up to 20 %).

The apparent elastic properties of the UD laminate under biaxial loading were extracted from the stress-strain curves in Fig. 4. The parameter E_2^α is used to denote the apparent transverse modulus for each loading angle and is plotted against α in Figure 5 and was calculated using a linear fit to the representative stress-strain curves shown in Figure 4 a and c in the strain range of 0.5 – 0.25 %. E_2^α is the greatest for the pure tension and pure compression stress states (*i.e.* α = 0° and 180°). For combined stress states where shear stress is applied in addition to tension/compression (loading angles α= 30°, 45°, 120°, 135°, 150° and 165°, see Fig. 5), E_2^α is reduced. In contrast, there is no significant change of the apparent shear modulus observed when transverse tension/compression stresses are superimposed.

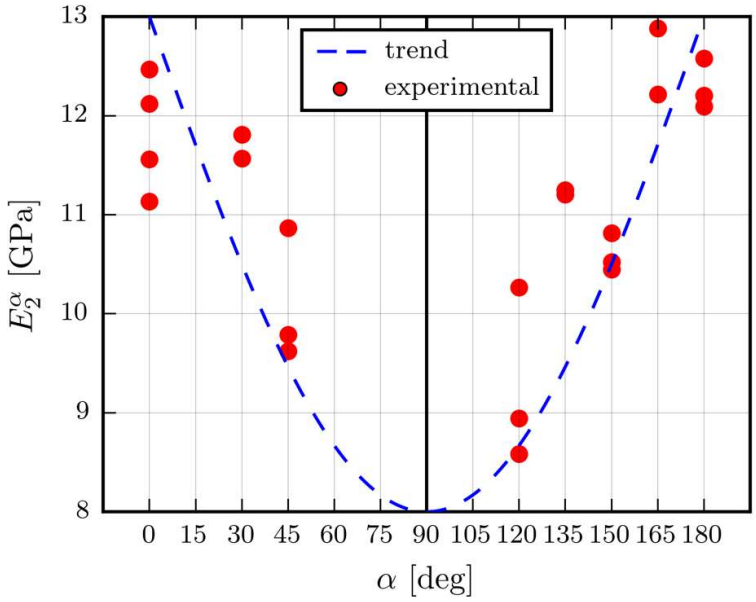

Fig.5: Dependency of the apparent transverse modulus on the loading angle α .

To verify the stress-strain curves measured with the MAF, the linear elastic properties extracted from the uniaxial MAF load cases (α= 0°, 90°, 180°) were compared against uniaxial tension, compression and shear ASTM standard test results (see Table 2). It was found that the MAF results agree reasonable well with the standard test results and the MAF/DIC approach is thus suitable to obtain the elastic properties used for this work. Furthermore, the nonlinear constitutive responses and the stress interaction effects obtained using the MAF also agreed well with similar biaxial experimental data found in the literature obtained using tubular specimens [22], [25].

Table 2: Comparison of uniaxial elastic properties for glass/epoxy RP-528 obtained from standard tests and the MAF.

	Standard Test			**MAF Test**	
Material Property	**Designation**	**Mean**	**c.v. [%]**	**Mean**	**c.v. [%]**
E_2^T [GPa]	ASTM D3039	10.94	3.13	11.51	1.66
E_2^C [GPa]	ASTM D3410	11.87	2.25	12.38	1.33
G_{12} [GPa]	ASTM D5379	3.60	2.68	3.48	2.47

3 Non-associative elasto-plastic material model

The total strain tensor $\boldsymbol{\epsilon}$ is decomposed into the sum of an elastic and a plastic strain component tensor following the classical plasticity theory as in *e.g.* [26]:

$$\boldsymbol{\epsilon} = \boldsymbol{\epsilon}^e + \boldsymbol{\epsilon}^p \tag{5}$$

where the superscripts *e* and *p* denote elastic and plastic components, respectively. The elastic constitutive law for a plane stress condition is expressed as:

$$\boldsymbol{\epsilon}^e = \mathbf{C}^e \boldsymbol{\sigma} \tag{6}$$

where $\mathbf{C}^e$ is the elastic compliance matrix for plane stress of an orthotropic composite lamina [27]. To model the plastic response of a transversely isotropic UD lamina, a yield function $f(\sigma_{ij})$ is defined based on stress invariants that remain unchanged for arbitrary rotations about the symmetry axis (*i.e.* the fibre *1*- direction) [5], [21], [28]:

$$\begin{aligned} I_1 &= \sigma_{11} \\ I_2 &= \sigma_{22} + \sigma_{33} \\ I_3 &= {\tau_{12}}^2 + {\tau_{13}}^2 \\ I_4 &= (\sigma_{22} - \sigma_{33})^2 + 4{\tau_{23}}^2 \\ I_5 &= (\sigma_{22} - \sigma_{33})({\tau_{13}}^2 - {\tau_{12}}^2) - 4\tau_{12}\tau_{13}\tau_{23} \end{aligned} \tag{7}$$

where the indices *1*, *2* and *3* refer to the directions parallel to the fibres, in-plane transverse to the fibres and out-of-plane transverse to the fibres, respectively (see Fig. 1). Based on the experimental observation that the constitutive response of a typical UD composite laminate is quasi linear elastic in the fibre direction, I_1 is excluded from the formulation of the yield function. From physical reasoning, the yield criterion should not depend on the sign of the shear stresses and therefore I_5 is excluded as well. Thus, for a general three-dimensional case, the following yield function similar to the Drucker-Prager model is proposed [5]:

$$f(\sigma_{ij}) = \sqrt{H(\sigma_{22} - \sigma_{33})^2 + L{\tau_{23}}^2 + M({\tau_{12}}^2 + {\tau_{13}}^2)} + J(\sigma_{22} + \sigma_{33}) \tag{8}$$

Equation (8) can be simplified for a 2D plane-stress condition by setting all out-of-plane stresses to zero, thus yielding:

$$f(\sigma_{ij}) = \sqrt{H\sigma_{22}{}^2 + \tau_{12}{}^2} + J\sigma_{22} \tag{9}$$

where H and J are plastic material coefficients that must be determined experimentally. According to [3], the shear coefficient M can be set to one without loss of generality. H controls the ellipticality of the yield surface in the σ_{22} versus τ_{12} stress space, *i.e.* when $H = 1$, the yield surfaces are circular. The coefficient J controls the sensitivity to hydrostatic stress and leads to a different response in transverse tension and compression. The special case of $J = 0$ implies that the material exhibits no pressure sensitivity, and thus that the transverse compressive and tensile yield behaviour are identical. To model plastic deformation and hardening in a complex three-dimensional stress state, a scalar effective plastic stress can be defined using the yield function:

$$\bar{\sigma} = f(\sigma_{ij}) \tag{10}$$

A non-associative plastic flow potential (*i.e.* plastic flow potential $g \neq$ yield function f) is proposed and defined in a similar way to the yield function in Equation (9), neglecting the pressure sensitive J term, *i.e.*:

$$\mathrm{g}(\sigma_{ij}) = \sqrt{H\sigma_{22}{}^2 + \tau_{12}{}^2} \tag{11}$$

The gradient of the potential function g defines the direction of the plastic flow increment (or plastic strain component vector) $d\epsilon_{ij}^p$:

$$d\epsilon_{ij}^p = \frac{\partial g(\sigma_{ij})}{\partial \sigma_{ij}} d\lambda \tag{12}$$

where $i, j = 1, 2, 3$ and where $d\lambda$ is the plastic multiplier.

For the pressure sensitive fibre reinforced polymer material, a non-associative flow rule is chosen over a simpler associative flow rule as the latter induces a non-physical constitutive behaviour for shear-dominated combined compression/shear stress states. This is illustrated in Fig. 6 by considering the case of pure shear loading (loading along vertical axis), chosen for clarity: when an associative flow rule is used, the resultant plastic strain vector as per definition will be normal to the yield surface (∇f), and non-physical positive plastic transverse strains, ϵ_{22}^p (red horizontal arrow in Fig. 6), are induced even for a pure shear stress state where no plastic transverse strains would be expected. Erroneous predictions will also be made for shear dominated combined compression/shear stress states (indicated by the transparent red triangle area in Fig. 6), since tensile rather than compressive plastic transverse strains are predicted. This physical inconsistency can be eliminated by adopting a non-associative flow rule (red ellipse in Fig. 6) by which the resulting plastic flow

direction (∇g) will be aligned purely along the vertical axis for pure shear stress states, and, as expected, the plastic transverse stresses for shear dominated combined compression/shear stress states will be compressive. An experimental example of this will be demonstrated and discussed in Section 5 of this paper. Thus, based on physical reasoning it is argued that an appropriate simple potential function for pressure sensitive materials, such as UD composites, should satisfy the symmetry condition:

$$\frac{\partial g(0,\tau_{12})}{\partial \sigma_{22}} = 0 \tag{13}$$

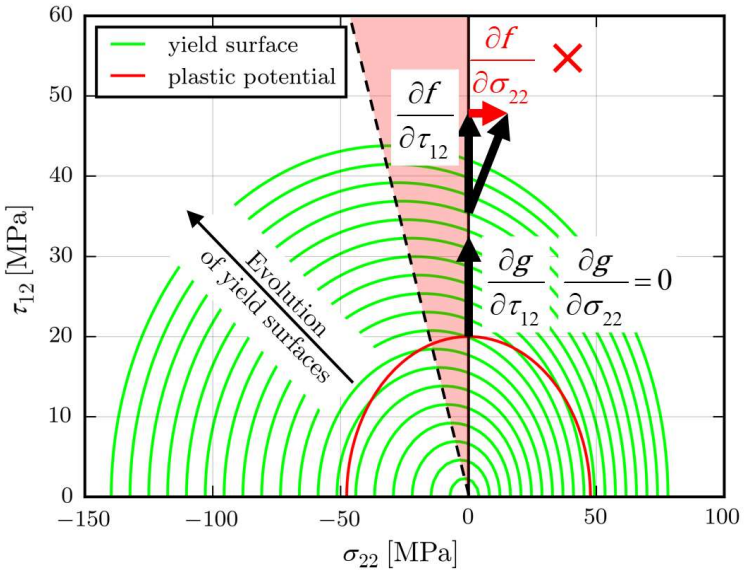

Fig. 6: Yield surfaces and plastic potential function of the non-associative plasticity model. Note that the number of yield surfaces shown and the size of the relative size of the potential and yield surfaces are purely illustrative.

Using the definition of the effective stress, $\bar{\sigma}$, given by Equation (10), the increment of equivalent plastic work per unit volume dW_P is expressed as:

$$dW_p = \sigma_{ij} d\epsilon_{ij}^p = \bar{\sigma} d\bar{\epsilon}^p \tag{14}$$

where $d\bar{\epsilon}^p$ is the increment of the effective plastic strain, and repeating indices imply Einstein summation. The plastic multiplier, $d\lambda$, can be found by substituting the plastic flow rule given in Equation (12) into Equation (14):

$$\sigma_{ij} \frac{\partial g(\sigma_{ij})}{\partial \sigma_{ij}} d\lambda = \bar{\sigma} d\bar{\epsilon}^p \Rightarrow g(\sigma_{ij}) d\lambda = f(\sigma_{ij}) d\bar{\epsilon}^p \tag{15}$$

Upon rearranging, $d\lambda$ is found as:

$$d\lambda = \frac{f(\sigma_{ij})}{g(\sigma_{ij})} d\bar{\epsilon}^p . \tag{16}$$

After inserting $d\lambda$ back into the plastic flow rule in Equation (12), and evaluating the partial derivatives of the potential function, the incremental plastic strain components, $d\epsilon_{ij}^{p}$, are obtained as follows.

$$\begin{Bmatrix} d\epsilon_{11}^{p} \\ d\epsilon_{22}^{p} \\ d\gamma_{12}^{p} \end{Bmatrix} = \begin{Bmatrix} 0 \\ (H\sigma_{22}^{2} + \tau_{12}^{2})^{-0.5} H\sigma_{22} \\ (H\sigma_{22}^{2} + \tau_{12}^{2})^{-0.5} \tau_{12} \end{Bmatrix} \frac{\mathrm{f}(\sigma_{ij})}{g(\sigma_{ij})} d\bar{\epsilon}^{p} . \tag{17}$$

It is implicitly assumed in the adopted plasticity model that a master effective plastic stress-strain curve (or hardening rule) exists, from which $d\bar{\epsilon}^{p}$ can be computed knowing $\bar{\sigma}$ from Equation (10). The relationship is approximated with the Ramberg-Osgood equation [29]:

$$\bar{\epsilon}^{p} = \left(\frac{\bar{\sigma}}{K}\right)^{1/m} \tag{18}$$

Thus, by substituting Equations (18) into (17), all the plastic strain components can be evaluated based on the stress state alone. The yield parameters (*H, J*) and the hardening parameters (*K, m*) remain to be determined experimentally. It should be emphasized that the adoption of a Ramberg-Osgood type description for the effective stress-strain relationship is merely based on phenomenological (rather than physically based) considerations to include the cumulative effects of (actual) material plasticity, micro-cracking and geometrically nonlinear effects as stated in section 1. Thus, Equation (18) does not represent 'hardening' in a conventional sense in the proposed formulation, but merely a suitable nonlinear relations between stress and effective plastic strain.

4 Model calibration using the MAF

The model is calibrated using the transverse and shear stress-strain curves shown in Fig. 4. To start with, the plastic strain components, $d\epsilon_{22}^{p}$ and $d\gamma_{12}^{p}$, are extracted from the total strains according to Equations (5) and (6) where the apparent Young's moduli as shown in Fig. 5 are used to compute the compliance matrix **C** for each individual biaxial load case. The effective plastic strain increment, $d\bar{\epsilon}^{p}$, can now be expressed as a function of *H* and *J* and based on the experimentally extracted plastic strain components upon rearranging the second and third rows respectively in Equation (17) to give:

$$\begin{aligned} d\bar{\epsilon}^{p} &= \frac{d\epsilon_{22}^{p}}{(\mathrm{H}\sigma_{22}{}^{2} + \tau_{12}{}^{2})^{-0.5} H\sigma_{22}} \frac{g(\sigma_{ij})}{f(\sigma_{ij})} \\ &= \frac{d\gamma_{12}^{p}}{(\mathrm{H}\sigma_{22}{}^{2} + \tau_{12}{}^{2})^{-0.5} \tau_{12}} \frac{g(\sigma_{ij})}{f(\sigma_{ij})} \end{aligned} \tag{19}$$

Note that by using Equation (19), two effective plastic strains (and thus two effective plastic stress-strain curves or hardening curves) can be defined for each load case based on the respective transverse and shear stress-strain curves. In an ideal scenario following the theory, the extracted

effective plastic strains from both equations would be identical and would exactly follow the effective plastic stress-strain curve defined in Equation (18). Thus, an optimisation procedure is adopted to find the best set of model parameters where the extracted effective plastic stress-strain curves both collapse on the same hardening curve. Therefore, a cost function is defined as the vector of the differences between the effective plastic strains extracted from the experimental stress-strain curves of every load case according to Equation (19) and the analytical effective plastic strains given by Equation (18). The optimised effective plasticity coefficients are then found by minimising the least-squares error of the cost function. In other words, the model is calibrated when the effective plastic stress-strain curves as a function of H and J collapse onto the hardening curve described by Equation (18). The optimisation was carried out using a purpose written Python code embedded in a least-squares optimisation algorithm [30].

Referring to Fig. 4, it is shown that the stress-strain curves obtained for compressive loading exhibit a distinct plateau region. The plateaued regions of the stress-strain curves were excluded from model calibration by identifying a strain cut-off point at the beginning of the plateau region as tabulated in Table 3. The exclusion of data points above the strain cut-off points is justified based on the fact that the adopted plasticity model framework loses its applicability (or physical suitability) at very large strains where macroscopic damage occurs due to stress concentrations around the notches of the specimen or out-of-plane geometrical instabilities.

Table 3: Strain cut-off points for stress strain curves obtained under compressive loading.

α [deg]	**120°**	**135°**	**150°**	**165°**	**180°**
Transverse strain cut-off point [-]	0.5 %	0.9 %	3.0 %	-	2 %
Shear strain cut-off point [-]	5.0 %	7.5 %	7.5 %	-	N/A

Fig. 7 shows the effective plastic stress-strain curves for the optimised/calibrated yield parameters where the experimental stress-strain curves of all load cases are included in the optimisation process (see No. 1 in Table 4). Fig.7 a and 7b shows the effective plastic stress-strain curves obtained from the transverse stress-strain curves and the shear stress-strain curves, respectively. The assumption of the existence of a master effective plastic stress-strain curve, which is independent of the biaxial stress state characterised by the loading angle α, is generally confirmed by the plots in Figs. 7a and 7b. It is possible to fit a Ramberg-Osgood equation similar to [2], [3] and [5], to the data with a correlation coefficient of $R^2 = 0.925$, thus demonstrating the suitability of the Ramberg-Osgood equation to describe the effective plastic stress-strain curves.

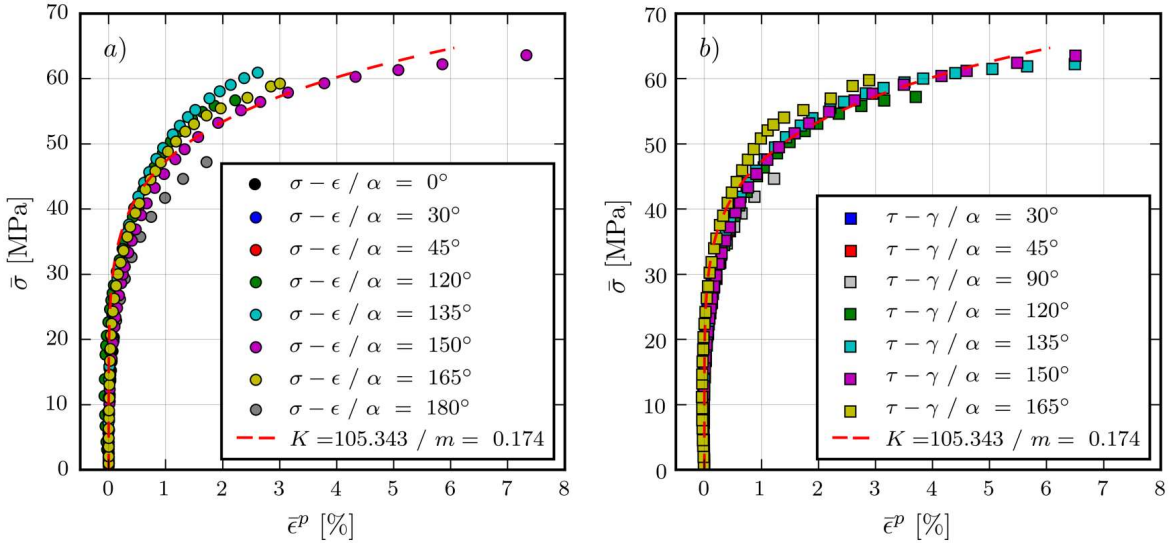

Fig. 7: Effective plastic stress-strain curves for all load cases obtained based on the transverse (a) and shear (b) stress-strain curves collapsed into a single master curve using the yield parameters from Table 4 (No. 1).

The acquisition of transverse normal and shear strains using DIC allows the computation of two effective plastic stress-strain curves per biaxial load case (see Fig 7a and 7b) which allows the verification of both plastic strain components individually. This is a major difference and improvement in comparison to the off-axis tests reported in the literature [2], [3], where only the on-axis stress-strain relationships in the direction of the applied load was obtained and verified. The individual contributions of the plastic transverse normal and shear strains are therefore obscured and cannot be fully verified independently. Having both the transverse and shear stress-strain curves is particularly important to highlight the superiority of the proposed non-associative flow rule over the associative one which will be demonstrated on experimental data in Section 5.

Table 4 presents the results of a sensitivity analysis investigating the influence of the choice of the load cases included in the optimisation procedure to identify the resultant plasticity model parameters and the corresponding model's predictive capability as indicated by the R^2 value. In calibration set No. 1 in Table 4, the stress-strain curves of all tested load cases were included in the optimisation procedure. In the cases of calibration sets No. 2 to 10, the number of load cases was systematically reduced to identify a) the lowest number of load cases needed, and b) the most suitable load cases to include in the model calibration to give good predictive capability. Furthermore, the sets No. 11 to 14 report the calibrated model parameters and predictive capability of using only uniaxial load cases.

Table 4: Sensitivity of the nonlinear material model parameters and the 'goodness of fit' on the choice of experimental data sets included in the parameter calibration/optimisation. .

No	**α's included**	**No. of α's**	***H* [-]**	***J* [-]**	***K* [MPa]**	***m* [-]**	**R^2**
1	All	9	0.190	0.069	105.3	0.174	0.925
2	All but 0°, 90°, 180°	6	0.183	0.058	108.4	0.178	0.916
3	30°, 120°, 135°, 150°, 165°	5	0.181	0.053	107.5	0.175	0.921
4	45°, 120°, 135°, 150°, 165°	5	0.183	0.058	108.4	0.178	0.916
5	45°, 120°, 150°, 165°	4	0.192	0.082	101.2	0.170	0.930
6	45°, 135°, 150°, 165°	4	0.197	0.075	95.7	0.146	0.940
7	45°, 135°, 150°	3	0.202	0.066	95.7	0.141	0.936
8	45°, 135°, 165°	3	0.189	0.083	95.7	0.148	0.917
9	45°, 135°	2	0.124	0.151	95.7	0.182	0.455
10	45°, 165°	2	0.207	0.137	94.832	0.175	0.882
11	0°, 90°, 180°	3	0.213	0.087	125.1	0.235	0.864
12	0°, 90°	2	0.306	0.175	105.5	0.200	0.812
13	90°, 180°	2	0.211	0.084	125.1	0.235	0.661
14	0°, 180°	2	0.463	0.072	95.686	0.048	N/A

Table 4 shows that the calibration sets No. 1 to 8 yield very similar model parameters (H = 0.181 – 0.202, J = 0.053 – 0.083, K = 95.7 – 108.4, m = 0.141 – 0.178) with a high predictive capability (R^2 > 0.9). This indicates that not all experimental data needs to be included in the optimisation. However, the sensitivity study has shown that it is advantageous to include at least three judiciously chosen load cases, *i.e.* one in tension/shear (α = 30°-, 45°), one in moderate compression/shear (α = 120°-, 135°) and one in compression dominated compression/shear (α = 150°-, 165°). This is because UD composites exhibit three distinctly different failure modes within the transverse tension/compression and shear stress space (*e.g.* the inter-fibre failure modes A, B and C as defined by Puck [22],[23]). Therefore, to achieve a good model calibration, it is necessary to select load cases which yield stress-strain curves that adequately represent the three distinct mechanical responses and failure mechanisms. Further, recalling the plasticity model framework in Fig. 6 and the yield function in Eqn. (9), it is clear that to determine the hydrostatic term J, which describes the offset of the centre point of the yield ellipse from the origin, it is required to include a tension/shear and a compression dominated load case to accurately locate the origin of the yield ellipse. On the other hand, to determine the coefficient H, which describes the ellipticality or transverse/shear anisotropy, a shear dominated load case is needed in addition. In summary, stress-strain curves derived for different biaxial stress states are required, which comprise different information regarding the mechanisms

that generate nonlinearity, to achieve a robust and overall accurate model calibration. The point is further demonstrated by the calibration sets of No. 9 to 14 in Table 4. Calibration set No. 9 fails to include sufficient information on the pressure sensitivity due to the omission of compression dominated load cases, resulting in poor predictive capability. Similarly, set No. 10 yields poor predictive capability because a shear dominated compression/shear load case is omitted and the ellipticality is not captured well in the included data. Calibration set No. 11, which includes all three uniaxial load cases, is also insufficient as the overall predictive capability is still poorer than when three biaxial load cases are used instead. The reason for this is that a uniaxial load case provides only one stress-strain curve for model calibration compared to two stress-strain curves for a biaxial load case. Finally, calibration sets No. 13, which does not include a tension/shear load case, and No. 14, without a shear dominated load case, both produce low R^2 values (*i.e.* poor model fit) due to insufficient information regarding the pressure sensitivity or anisotropy, respectively.

The predicted stress-strain curves, using the optimised parameters from No. 1 in Table 4, are compared against the experimental data in Fig. 8. The predicted normal and shear stress-strain curves match well with the experimental data. In the cases of combined tension/shear (Fig. 8a and b) the plastic strains are generally under predicted by the model. However, in comparison to linear elastic analysis, the strain predictions are greatly improved and the general behaviour is well predicted, *i.e.* the level of plasticity increases with increased loading angle α. For combined compression/shear stress states, the transverse stress-strain curves for $\alpha = 120°$ and 165° are in excellent agreement with the experimental data. For $\alpha = 135°$ the plastic strains are slightly over-predicted, while for $\alpha = 180°$ and $\alpha = 150°$ slightly under-predicted (see Fig. 8c). The predicted shear stress-strain curves are generally in good agreement with the experimental data except for pure shear ($\alpha = 90°$) where the plastic shear strains are under predicted (see Fig. 8d).

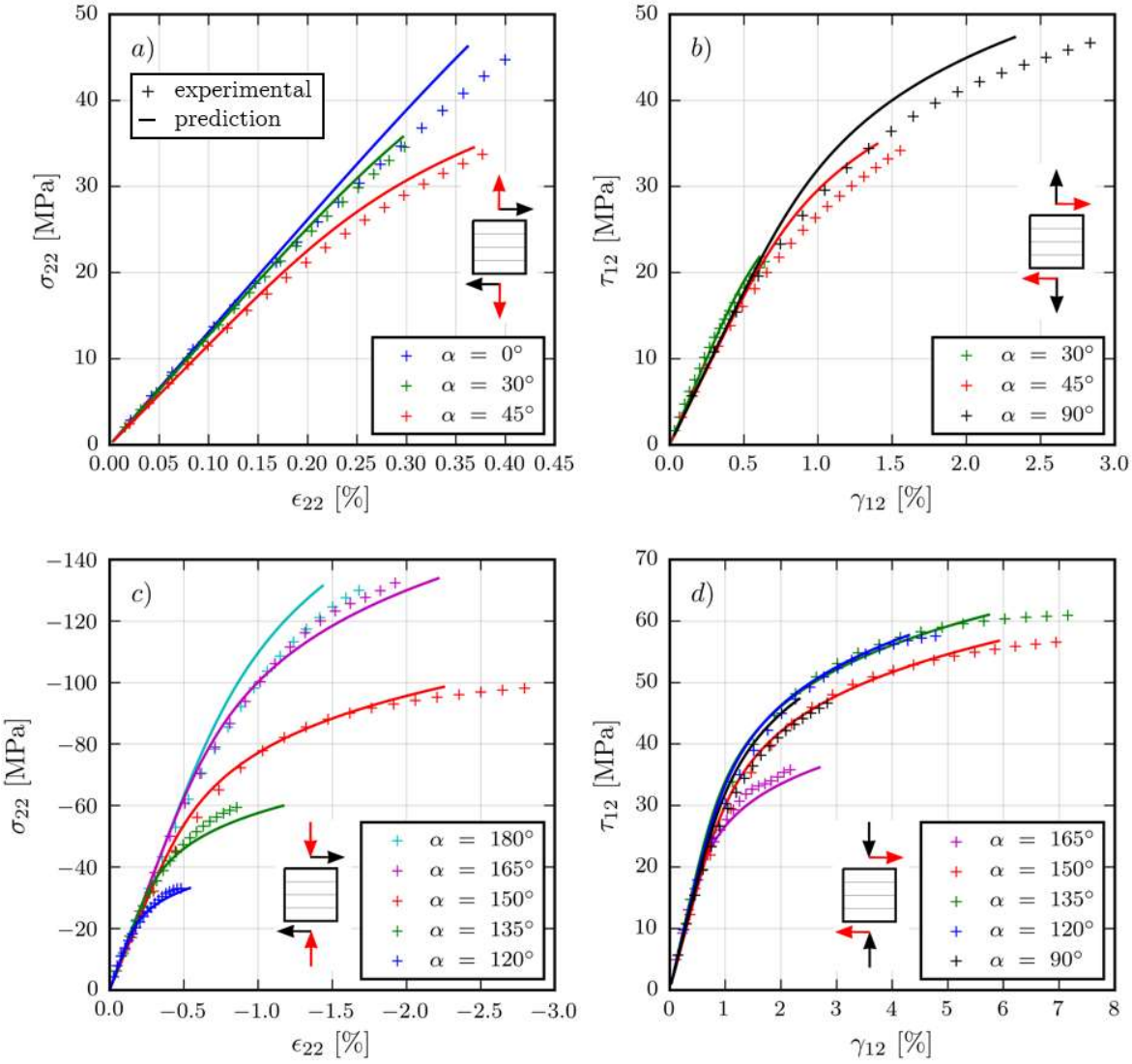

Fig. 8: Non-associative plasticity model predictions in comparison to MAF experimental data. Note that the small figure inserts illustrate the stress state, while the corresponding strain component is highlighted in red.

5 Model calibration using off-axis test results from the literature

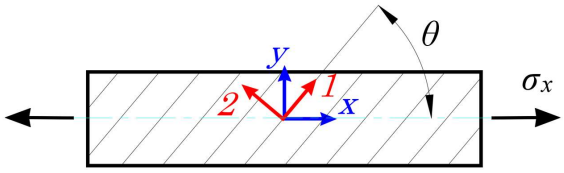

Fig. 9: Illustration of an off-axis test and definition of the off-axis angle θ and the nominal stress σ_x.

In this section, the non-associative plasticity model was applied to off-axis tension/compression experimental data for T800/3633 carbon/epoxy [2] and infused glass/epoxy [20], respectively. Fig. 9 illustrates a uniaxially loaded off-axis UD specimen where the off-axis angle θ relates the nominal stress σ_x to the local (lamina) stress state through:

$$\begin{aligned}\sigma_{11} &= \sigma_x \cos^2(\theta)\\ \sigma_{22} &= \sigma_x \sin^2(\theta)\\ \tau_{12} &= -\sigma_x \sin(\theta)\cos(\theta)\end{aligned} \tag{20}$$

The off-axis angle θ determines the biaxial stress state similar to the MAF loading angle α (see Fig. 1a), which is related to θ through the following relationship:

$$\theta = \begin{cases} 90° - \alpha, \sigma_x \geq 0 \\ -90° + \alpha, \sigma_x \leq 0 \end{cases} \tag{21}$$

where small off-axis angles θ correspond to shear dominated load cases and MAF loading angles α close to pure shear loading (α = 90°). The reported stress-strain curves for various off-axis angles were digitised. The plasticity models were then calibrated by collapsing all the effective plastic stress-strain curves from the different load cases (stress states) into one master curve to which Equation (18) was fitted. Fig. 10 shows the best fit effective plastic stress-strain curves obtained with the optimised plasticity parameters given in Table 5, where *'t'* and *'c'* in the legends represent tensile and compressive off-axis test data, respectively. From Fig. 10, and based on the R^2 values of 0.978 and 0.950 given in Table 5, it is clearly shown that the predicted master effective plastic stress-strain curve fits the experimental stress-strain data well for both material systems, and thus is suitable to describe their nonlinear behaviour. For the case of the off-axis tests presented in [2] and [20], only one effective plastic stress-strain curve can be extracted per off-axis angle from the experimentally obtained stress-strain curve (σ_x versus ϵ_x) in the global loading direction. This is different to the MAF/DIC approach discussed in the previous section, where the effective plastic stress-strain curves can be obtained from the transverse and shear stress-strain curves independently (see Equation (19) and Fig. 7). The additional information allows verification of not only the overall induced nonlinear behaviour, but also of the prediction of the individual plastic strain components. The transformation of local off-axis stress and strain to global off-axis stress and strain, and the steps required to calibrate the proposed non-associative plasticity model from off-axis test data, are given in the Appendix.

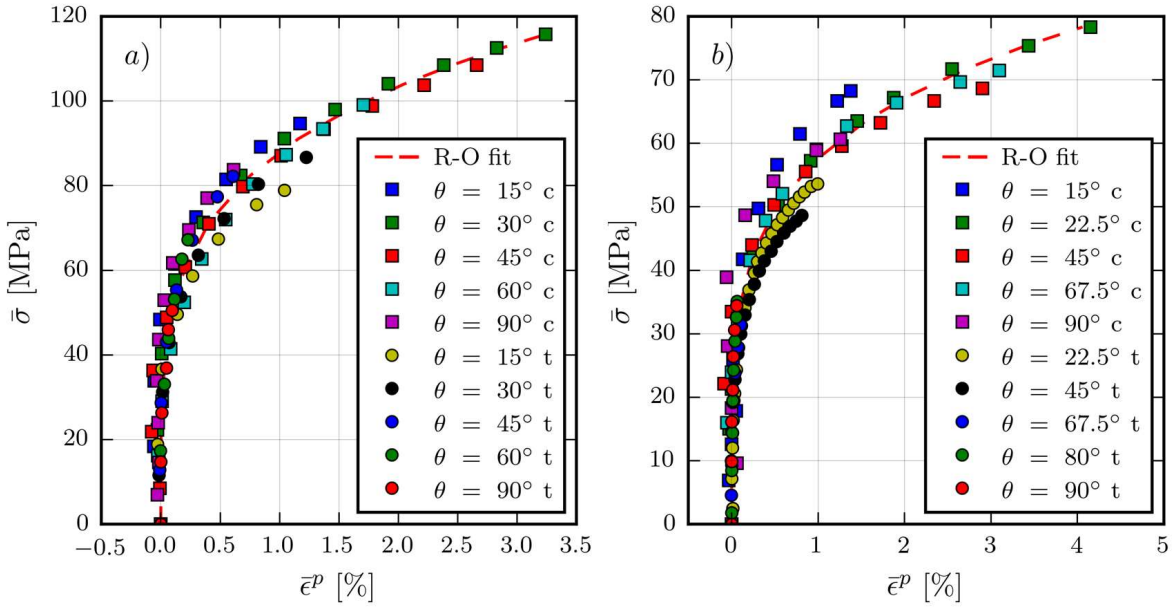

Fig. 10: Effective plastic stress-strain curves after least-squares optimisation for T800/3633 carbon/epoxy [2] *(a) and infused glass/epoxy* [20] *(b) showing the Ramberg-Osgood fit (R-O fit).*

Table 5: Calibrated plasticity parameters for the developed non-associative model.

Material	***H* [-]**	***J* [-]**	***K* [MPa]**	***m* [-]**	R^2
T800/3633 [2]	0.319	0.132	257.346	0.233	0.978
glass/epoxy [20]	0.355	0.212	151.149	0.209	0.950

For comparison, the associative plasticity model proposed in [2] was also calibrated using the same data sets and the optimum plasticity parameters are given in Table 6 adopting the notation as defined in [2], where *a1* and *a66* are yield parameters similar to *H* and *J*, and *A* and *n* are fitting parameters similar to *K* and *m*.

Table 6: Calibrated plasticity parameter for the associative model [2].

Material	***a1* [-]**	***a66* [-]**	***A* [1/MPa]**	***n* [-]**	R^2
T800/3633 [2]	0.09*	2.7*	3.14e-13*	4.19*	0.979
glass/epoxy [20]	0.129	3.931	1.528e-13	4.51	0.947
* Values directly taken from [2]					

Both the predictions of off-axis stress-strain curves by the proposed non-associative plasticity model and the reference associative model [2] are plotted and compared against experimental results for carbon/epoxy [2] in Fig. 11 and for vacuum infused glass/epoxy in Fig. 12 [20].

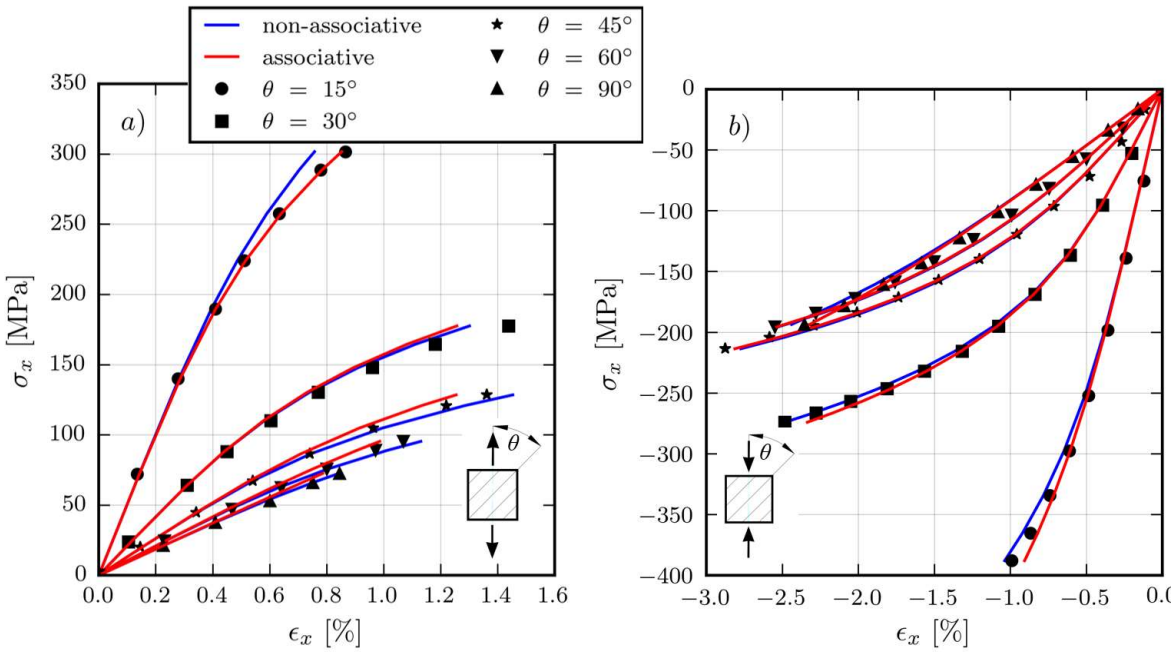

Fig. 11: Carbon/epoxy T800/3633 tensile (a) and compressive (b) off-axis experimental results (data points) [2] *compared against model predictions (solid lines). The small figure inserts illustrate the stress state and the off-axis angle.*

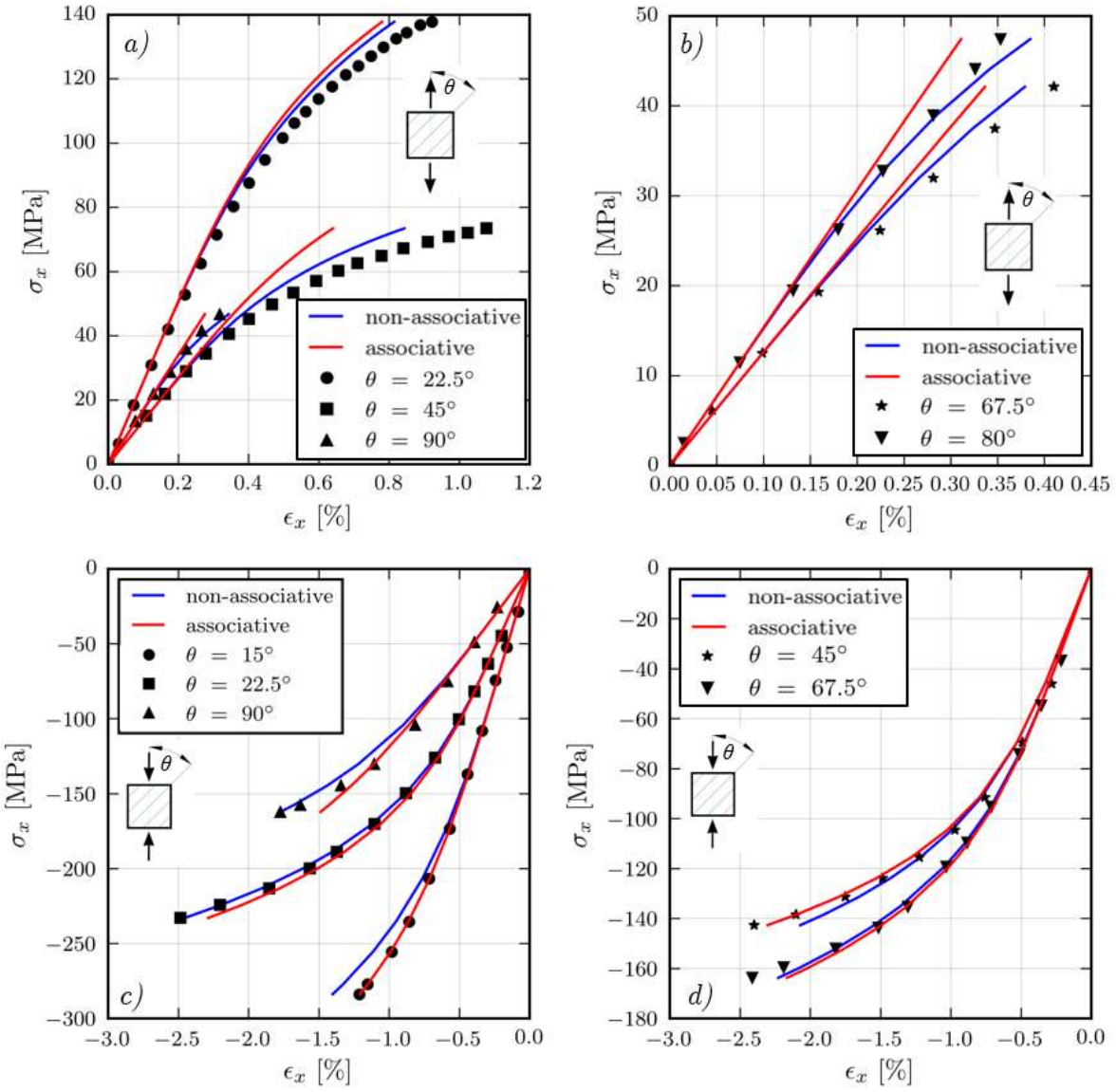

Fig. 12: Vacuum infused glass/epoxy tensile (a and b) and compressive (c and d) off-axis experimental results (data points) [20] *compared against model predictions (solid lines). The curves are plotted in different figures for clarity. The small figure inserts illustrate the stress state and the off-axis angle.*

Fig. 11 and 12 show that both models (associative and non-associative) predict the nonlinear off-axis stress-strain curves for both material systems in good agreement with the experimental data and with a similar degree of accuracy (see R^2 in Tables 3 and 4). It is not apparent that the proposed non-associative plasticity model gives better predictions than the associative model as the subtle differences are obscured in the on-axis plastic strains, which are a function of the transverse normal and shear strain components in the local *1,2*- coordinate system.

To illustrate the advantages and physical consistency of the proposed non-associative plasticity model over the associative models, the components of the plastic strains (ϵ_{22}^p and γ_{12}^p) predicted by the proposed non-associative model and the associative model of [2] are plotted individually against the off-axis stress σ_x in Fig. 13 for selected compressive load cases for carbon/epoxy T800/3336 (same qualitative results apply to glass/epoxy). Both models predict similar plastic shear strain components

γ_{12}^p (Fig 13b), with the associative model giving slightly lower values. However, the plastic transverse strains ϵ_{22}^p predicted by the two models are different (see Fig 13a). The associative model predicts tensile plastic transverse strains although the loading is compressive for off-axis angles $\theta = 15°$ and $\theta = 45°$ (see Fig. 13a), which is clearly non-physical. In contrast, the non-associative model predicts the plastic transverse strain to be compressive, as would be expected under compressive loading. This non-physical characteristic of the associative flow rule when used together with a Drucker-Prager type yield surface was also explained and illustrated in Fig. 6 (Section 3), and is a consequence of the negative slope of the yield surfaces in the case of pure shear and shear-dominated combined compression/shear stress states. Thus, adoption of an associative flow-rule forces the prediction of non-physical transverse strains for these stress states, hence a non-associative flow rule is required.

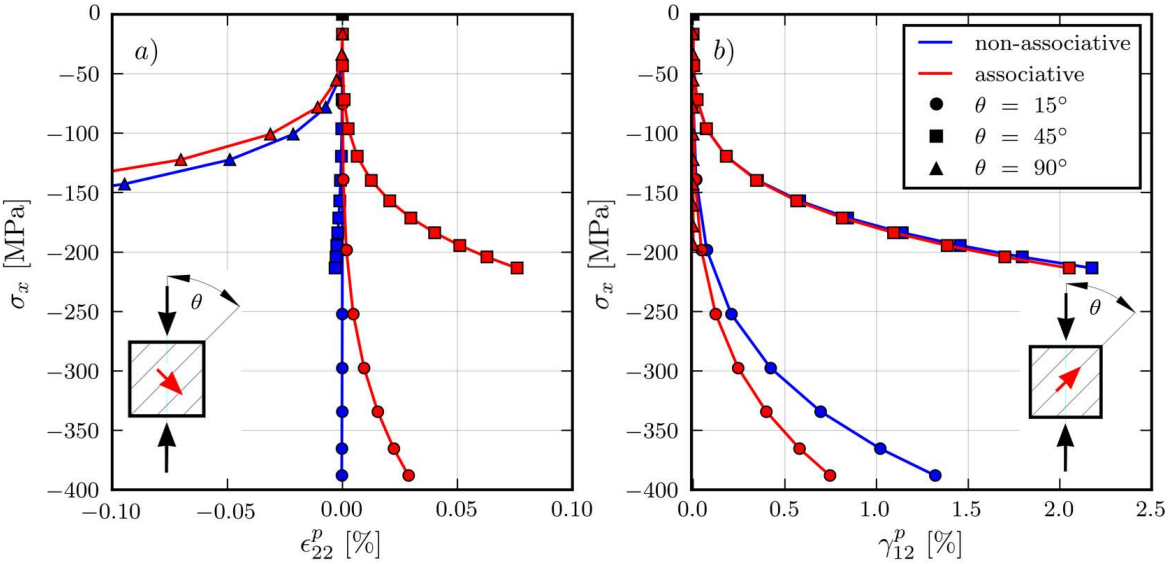

Fig. 13: Plastic component strains ϵ_{22}^p (a) and γ_{12}^p (b) as predicted by the non-associative (blue) and associative (red) models for compressive off-axis test on T800-3633 carbon/epoxy [2].

The comparison between the individual strain components predicted by the non-associative and the associative models in off-axis tests has clearly shown that the use of a non-associative flow rule is crucial to predict the effective plastic component strains correctly when a Drucker-Prager type yield surface is adopted. Furthermore, the study has demonstrated that it is important to obtain all the strain components experimentally, as facilitated by the MAF combined with DIC which provides full field strain maps. This enables full scrutiny, calibration and verification of nonlinear constitutive models, wheras simple axial and transverse strain measurements reported in most off-axis tests [2],[20] cannot achieve this.

6 Conclusions

A simple non-associative plasticity model based on the invariants of transverse isotropy has been developed for UD composite materials subjected to multiaxial in-plane loading. The model accounts for the cumulative nonlinear response due to resin plasticity, micro-cracking and geometrically nonlinear effects in the transverse and shear stress-strain curves, while assuming linear elastic behaviour in the fibre direction. The pressure dependent responses for transverse tension and compression stress states are accounted for using a Drucker-Prager type yield function.

The biaxial experimental data required to calibrate the model was obtained using a novel Modified Arcan Fixture (MAF) in combination with DIC. It has been shown that the MAF/DIC approach used is a viable and attractive alternative to conventional off-axis tests, experiments using tubular composite specimens, experiments in high-pressure chambers, or experiments involving multiple actuators, to generate biaxial experimental data for nonlinear constitutive model calibration. The advantages of the MAF approach are that the specimens are inexpensive, easy to manufacture and closely resemble the flat (or nearly flat) composite laminates used in most structural applications (unlike tubular specimens), and that the tests can be conducted on a standard test machine without the need for an additional actuator. The model is calibrated by minimising the difference between the experimentally extracted effective plastic stress-strain curves and the nonlinear relationship between stress and effective plastic strain described by the Ramberg-Osgood equation. It has been found that at least three judiciously chosen biaxial load cases should be used for model calibration; one in tension/shear, one in moderate compression/shear, and one in compression dominated compression/shear.

The model has been applied to a glass/epoxy prepreg material system tested using the MAF. The analysis of the MAF experimental data has shown that the nonlinearities in all the measured transverse and shear stress-strain curves corresponding to different biaxial stress states can be reduced into a single effective plastic stress-strain curve. By adopting a plasticity modelling framework to account for the nonlinear material behaviour, it is demonstrated that an associative flow rule, when used with a pressure sensitive Drucker-Prager type yield function, can induce incorrect, non-physical plastic transverse strains for pure shear and shear-dominated combined compression/shear stress states. However, the issue can be resolved by adopting a non-associative model. The research conducted has shown the importance of measuring all the strain components experimentally for full model calibration, *e.g.* using a full-field DIC approach, to ensure that the predicted individual plastic strain components can be verified.

The model was further verified against off-axis experimental data from the literature for an infused glass/epoxy and a carbon/epoxy material system. The predicted off-axis stress-strain curves agreed well with the experimental results. Thus, it has been shown that the proposed non-associative

plasticity model is applicable to a wide range of advanced composites. Further, the model can be implemented in a finite element framework for detailed nonlinear stress and strain analyses in composite components and structures subjected to multiaxial loading. This will be pursued in continuation of this research.

Acknowledgements

The research is supported by the EPSRC Doctoral Training Grant. The secondment of the first author to the University of Southampton Malaysia, where a part of this research was conducted, is supported by the Fundamental Research Grant Scheme (FRGS/1/2015/TK09/USMC/03/1) of the Ministry of Higher Education of Malaysia. The first author acknowledges the support received through a Stanley Gray Fellowship granted by the Institute of Marine Engineering, Science and Technology (IMarEST).

References

[1] Composite Leadership Forum, “The 2016 UK Composites Strategy,” 2016.

[2] T. Yokozeki, S. Ogihara, S. Yoshida, and T. Ogasawara, “Simple constitutive model for nonlinear response of fiber-reinforced composites with loading-directional dependence,” *Compos. Sci. Technol.*, vol. 67, no. 1, pp. 111–118, 2007.

[3] C. T. Sun and J. L. Chen, “A simple flow rule for characterizing nonlinear behavior of fiber composites,” *J. Compos. Mater.*, vol. 23, no. 10, pp. 1009–1020, 1989.

[4] D. C. Drucker and W. Prager, “Soil mechanics and plastic analysis or limit design,” *Q. Appl. Math.*, vol. 10, no. 2, pp. 157–165, 1952.

[5] K. W. Gan, M. R. Wisnom, S. R. Hallett, and G. Allegri, “A simple plasticity model for predicting transverse composite response and failure,” in *The Proceedings of the 19th international conference on composite materials*, 2013.

[6] J. P. Boehler and A. Sawaczuk, “Application of representation theorems to describe yielding of transversely isotropic solids,” *Mech. Res. Comun.*, vol. 3, pp. 277–283, 1976.

[7] A. J. M. Spencer, “Plasticity theory for fibre-reinforced composites,” *J. Eng. Math.*, vol. 26, no. 1, pp. 107–118, 1992.

[8] M. Vogler, R. Rolfes, and P. P. Camanho, “Modeling the inelastic deformation and fracture of polymer composites-Part I: Plasticity model,” *Mech. Mater.*, vol. 59, pp. 50–64, 2013.

[9] P. P. Camanho, M. A. Bessa, G. Catalanotti, M. Vogler, and R. Rolfes, “Modeling the inelastic deformation and fracture of polymer composites – Part II: Smeared crack model,” *Mech. Mater.*, vol. 59, pp. 36–49, 2013.

[10] K. D. Pae and K. Y. Rhee, “Effects of hydrostatic pressure on the compressive behavior of thick laminated 45 ° and 90 ° unidirectional graphite-fiber/epoxy-matrix composites,” *Compos. Sci. Technol.*, vol. 53, no. 3, pp. 281–287, 1995.

[11] G. M. Vyas, S. T. Pinho, and P. Robinson, “Constitutive modelling of fibre-reinforced composites with unidirectional plies using a plasticity-based approach,” *Compos. Sci. Technol.*, vol. 71, no. 8, pp. 1068–1074, 2011.

[12] E. S. Shin and K. D. Pae, “Effects of hydrostatic-pressure on the torsional shear behavior of graphite epoxy composites,” *J. Compos. Mater.*, vol. 26, no. 4, pp. 462–485, 1992.

[13] P. J. Hine, R. A. Duckett, A. S. Kaddour, M. J. Hinton, and G. M. Wells, "The effect of hydrostatic pressure on the mechanical properties of glass fibre/epoxy unidirectional composites," *Compos. Part A Appl. Sci. Manuf.*, vol. 36, no. 2 SPEC. ISS., pp. 279–289, 2005.

[14] S. Y. Hsu, T. J. Vogler, and S. Kyriakides, "Inelastic behavior of an AS4/PEEK composite under combined transverse compression and shear. Part II: Modeling," *Int. J. Plast.*, vol. 15, no. 8, pp. 807–836, 1999.

[15] T. J. Vogler and S. Kyriakides, "Inelastic behavior of an AS4/PEEK composite under combined transverse compression and shear. Part I: experiments," *Int. J. Plast.*, vol. 15, no. 8, pp. 783–806, 1999.

[16] M. A. Sutton, J. J. Orteu, and H. Schreier, *Image correlation for shape, motion and deformation measurements*. Springer, 2009.

[17] K. W. Gan, T. Laux, S. T. Taher, J. M. Dulieu-Barton, and O. T. Thomsen, "A novel fixture for determining the tension/compression-shear failure envelope of multidirectional composite laminates," *Compos. Struct.*, vol. 184, no. August 2017, pp. 662–673, 2018.

[18] M. Arcan, Z. Hashin, and A. Voloshin, "A method to produce uniform plane-stress states with applications to fiber-reinforced materials - A specially designed specimen yields material properties under pure shear or uniform plane-stress conditions," *Exp. Mech.*, vol. 18, no. 4, pp. 141–146, 1978.

[19] PRF Composites Materials, "Product data prepreg systems RP-528." [Online]. Available: http://www.prfcomposites.com/. [Accessed: 20-Sep-2016].

[20] S. Laustsen, E. Lund, L. Kühlmeier, and O. T. Thomsen, "Interfibre failure characterisation of unidirectional and triax glass fibre non-crimp fabric reinforced epoxy laminates," *Appl. Compos. Mater.*, vol. 22, no. 1, pp. 51–79, 2014.

[21] R. Cuntze, "The predictive capability of failure mode concept-based strength conditions for laminates composed of unidirectional laminae under static triaxial stress states," *J. Compos. Mater.*, vol. 46, no. 19–20, pp. 2563–2594, 2012.

[22] A. Puck and H. Schürmann, "Failure analysis of FRP laminates by means of physically based phenomenological models," *Compos. Sci. Technol.*, vol. 58, pp. 1045–1067, 1996.

[23] A. Puck and H. Schürmann, "Failure analysis of FRP lamninates by means of physically based phenomenological models," *Compos. Sci. Technol.*, vol. 62, pp. 1633–1662, 2002.

[24] C. G. Davila, P. P. Camanho, and C. A. Rose, "Failure criteria for FRP laminates," *J. Compos. Mater.*, vol. 39, no. 4, pp. 323–345, 2005.

[25] S. R. Swanson, M. J. Messick, and Z. Tian, "Failure of carbon / epoxy lamina under combined stress," *J. Compos. Mater.*, vol. 21, pp. 619–630, 1986.

[26] E. de S. Nato, D. Peric, and O. DRJ, *Computational methods for plasticity-Theory and Applications*. Chichester: Wiley, 2008.

[27] I. M. Daniel, *Engineering mechanics of composite materials*, 2nd ed. New York: Oxford University Press, 2005.

[28] P. P. Camanho, A. Arteiro, A. R. Melro, G. Catalanotti, and M. Vogler, "Three-dimensional invariant-based failure criteria for fibre-reinforced composites," *Int. J. Solids Struct.*, vol. 55, pp. 92–107, 2015.

[29] W.Ramberg and W.Osgood, "Description of stress-strain curves by three parameters," 1943.

[30] E. Jones, T. Oliphant, and P. Peterson, "SciPy Open source scientific tools for Python." 2001.

Appendix – Non-associative plasticity model calibration from off-axis tests

In the following, equations are derived that relate the effective plastic stress, $\bar{\sigma}$, and strain, $\bar{\epsilon}_p$, in an off-axis experiment to the measured stress σ_x and strain ϵ_x^{tot} in the loading direction (see Fig. 9). The derivation closely follows [2] but differs due to the adoption of a non-associative rather than an associative flow rule. The experimentally measured plastic strain in the loading direction ϵ_x^p is obtained as:

$$\epsilon_x^p = \epsilon_x^{tot} - \frac{\sigma_x}{E_x} \tag{A.1}$$

where E_x is the laminate modulus in the loading direction. The off-axis plastic strain ϵ_x^p can be expressed based on the local (lamina) strain components as:

$$\epsilon_x^p = \epsilon_{11}^p \cos^2(\theta) + \epsilon_{22}^p \sin^2(\theta) - \gamma_{12}^p \sin(\theta)\cos(\theta) \tag{A.2}$$

To simplify the derivation, $h(\theta)$ is defined by inserting the stress transformation rules in Equations (20) into the yield function in equation (9):

$$h(\theta) = \begin{cases} \sqrt{H \sin^4(\theta) + \sin^2(\theta)\cos^2(\theta)}, \sigma_x \geq 0 \\ -\sqrt{H \sin^4(\theta) + \sin^2(\theta)\cos^2(\theta)}, \sigma_x \leq 0 \end{cases} \tag{A.3}$$

Note, that by multiplying *h(θ)* with σ_x the yield function is retrieved.

The individual plastic strain components ϵ_{11}^p, ϵ_{22}^p and γ_{12}^p in Equation A.2 can be substituted by the expressions given in Equation (17). Then the transformed stresses from Equation (20) and *h(θ)* defined in Equation A.3 can be substituted and $\bar{\epsilon}^p$ is obtained as a function of σ_x, *h(θ)*, $f(\sigma_{ij})$ and $g(\sigma_{ij})$ upon rearranging:

$$\bar{\epsilon}^p = \frac{\epsilon_x^p}{h(\theta)} \frac{g(\sigma_{ij})}{f(\sigma_{ij})} \tag{A.4}$$

where

$$\frac{g(\sigma_{ij})}{f(\sigma_{ij})} = \frac{h(\theta)}{h(\theta) + J \sin^2(\theta)} \tag{A.5}$$

Inserting equation (A.5) into equation (A.4) one obtains:

$$\bar{\epsilon}^p = \frac{\epsilon_x^p}{h(\theta) + J \sin^2(\theta)} \tag{A.6}$$

Similarly, the effective plastic stress can be obtained as a function of σ_x as follows:

$$\bar{\sigma} = (h(\theta) + J\sin^2(\theta))\sigma_x \tag{A.7}$$

The model can now be optimised based on the derived effective plastic stress-strain curve in equation (A.6) and (A.7).